JOURNAL OF SYNCHROTRON RADIATION

ISSN 1600-5775

Received 23 February 2020
Accepted 31 July 2020

Edited by V. Favre-Nicolin, CEA and Université Joseph Fourier, France

Keywords: oxides; radiation damage; Monte Carlo method; finite element method; X-ray nanopatterning.

Supporting information: this article has supporting information at journals.iucr.org/s

Time and space resolved modelling of the heating induced by synchrotron X-ray nanobeams

Valentina Bonino,[a,b]* Daniele Torsello,[c,d] Carmelo Prestipino,[e] Lorenzo Mino[f] and Marco Truccato[b,c]

[a]ESRF – The European Synchrotron, 71 Avenue des Martyrs, 38000 Grenoble, France, [b]Department of Physics, University of Torino, via P. Giuria 1, 10125 Torino, Italy, [c]Istituto Nazionale di Fisica Nucleare, Sezione di Torino I, 10125 Torino, Italy, [d]Department of Applied Science and Technology, Politecnico di Torino, Torino 10129, Italy, [e]Institut Sciences Chimiques de Rennes, UMR-CNRS 6226, Campus de Beaulieu, Université de Rennes 1, 35042 Rennes Cedex, France, and [f]Department of Chemistry and Interdepartmental Centre NIS, University of Torino, via P. Giuria 7, 10125 Torino, Italy. *Correspondence e-mail: valentina.bonino@esrf.fr

X-ray synchrotron sources, possessing high power density, nanometric spot size and short pulse duration, are extending their application frontiers up to the exploration of direct matter modification. In this field, the use of atomistic and continuum models is now becoming fundamental in the simulation of the photoinduced excitation states and eventually in the phase transition triggered by intense X-rays. In this work, the X-ray heating phenomenon is studied by coupling the Monte Carlo method (MC) with the Fourier heat equation, to first calculate the distribution of the energy absorbed by the systems and finally to predict the heating distribution and evolution. The results of the proposed model are also compared with those obtained removing the explicit definition of the energy distribution, as calculated by the MC. A good approximation of experimental thermal measurements produced irradiating a millimetric glass bead is found for both of the proposed models. A further step towards more complex systems is carried out, including in the models the different time patterns of the source, as determined by the filling modes of the synchrotron storage ring. The two models are applied in three prediction cases, in which the heating produced in $Bi_2Sr_2CaCu_2O_{8+\delta}$ microcrystals by means of nanopatterning experiments with intense hard X-ray nanobeams is calculated. It is demonstrated that the temperature evolution is strictly connected to the filling mode of the storage ring. By coupling the MC with the heat equation, X-ray pulses that are 48 ps long, possessing an instantaneous photon flux of $\sim 44 \times 10^{13}$ photons s^{-1}, were found to be able to induce a maximum temperature increase of 42 K, after a time of 350 ps. Inversely, by ignoring the energy redistribution calculated with the MC, peaks temperatures up to hundreds of degrees higher were found. These results highlight the importance of the energy redistribution operated by primary and secondary electrons in the theoretical simulation of the X-ray heating effects.

1. Introduction

Since the first-generation synchrotrons, X-ray source characteristics have evolved under the strong demand for higher and higher spatial and temporal resolution. Today, peak brilliances up to 10^{26} photons s^{-1} mm^{-2} $mrad^{-2}$ (0.1% bandwidth)$^{-1}$ are achieved with third-generation synchrotron sources, and X-ray beams with nanometric spot sizes of ~50–100 nm and pulses of hundreds of photons s^{-1} with energies in the pJ range are routinely achieved (Mino *et al.*, 2018; Martínez-Criado *et al.*, 2016). However, the downside of this ongoing evolution of X-ray sources is that such beam characteristics can exceed the threshold where photon-flux density can affect the organization of matter (Bras & Stanley, 2016).

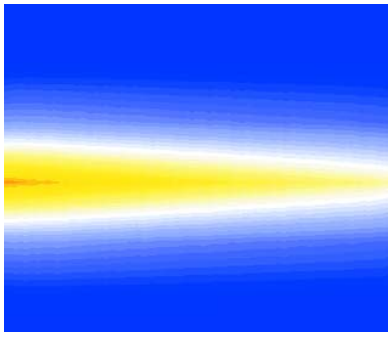

As a consequence, the displays of synchrotron X-ray beams inducing modification phenomena in inorganic materials, such as phase transitions (Adriaens *et al.*, 2013), reduction (Stanley *et al.*, 2014) and crystallization (Feldman *et al.*, 2009; Martis *et al.*, 2011), are now increasing in number. The X-ray heating effect is frequently claimed as a possible modification mechanism. So far, however, only a few experimental attempts have been made to clarify this point. For example, in two thermal-imaging experiments (Rosenthal *et al.*, 2014; Snell *et al.*, 2007) carried out on glass beads and on an indium microsized particle, X-ray heating up to ∼30 and 0.2° have been recorded, respectively.

Although more experimental efforts are needed in this direction, new research fields are emerging in which X-ray probing and material modification are strictly correlated (Tu *et al.*, 2017; Hsu *et al.*, 2015; Bonino *et al.*, 2019; Pagliero *et al.*, 2014; Truccato *et al.*, 2016; Mino *et al.*, 2017, 2019). In this background, we have recently demonstrated the feasibility of a new patterning concept, based on a resist-free method, which exploits the structural and electrical modifications induced in condensed matter by high-intensity nanometric beams from third-generation synchrotrons (Bonino *et al.*, 2019; Pagliero *et al.*, 2014; Truccato *et al.*, 2016; Mino *et al.*, 2017, 2019). For example, by irradiating the high-temperature superconductors $Bi_2Sr_2CaCu_2O_{8+\delta}$ and $YBa_2Ca_3O_{7-\delta}$ with a 17 keV nanobeam with a flux of $\sim 10^{11}$ photons s^{-1}, a change in the electrical behaviour was related to an increase in the crystal mosaicity and a depletion of the doping oxygen content (Bonino *et al.*, 2018, 2019). Following these findings, we exploited these local modifications to nanopattern three $Bi_2Sr_2CaCu_2O_{8+\delta}$ microcrystals, finally fabricating electrical devices based on the Josephson effect (Pagliero *et al.*, 2014; Truccato *et al.*, 2016; Mino *et al.*, 2017).

Despite all the experimental displays of photoinduced phenomena, owing to the large variety of X-ray–matter interaction mechanisms that can be accessed with high-intensity X-rays, a clear picture of the mechanisms involved in material modification is still missing. Depending on the beam intensity and pulse duration, both reversible and irreversible matter states can be induced in a variety of inorganic materials (London *et al.*, 2001; Hau-Riege, 2012). This is not surprising; indeed similar concepts have been extensively investigated in the field of high-power laser irradiation, where both thermal and non-thermal effects are currently exploited in many laser-based technological processes (Mirzoev *et al.*, 1996; Liu *et al.*, 1997).

The similarities between high-intensity synchrotron X-ray and optical and IR laser irradiations are several. As in femtosecond lasers, X-rays ionize the matter, but, differently from them, they excite the inner shells of the atoms and penetrate in-depth into the material volume. In the femtosecond scale, the absorbed X-ray energy is dissipated through the emission of fluorescent photons and Auger and photoelectrons. Then a cascade of excitation processes is initiated by electrons and eventually, in the picosecond timescale, they thermalize firstly among themselves and then with the lattice. Another difference with lasers concerns the surface power densities that can be delivered with a single pulse. Femtosecond lasers can reach 10^{22} W cm^{-2} (Bahk *et al.*, 2004), while the picosecond pulses of third-generation synchrotrons can only achieve values in the order of 10^{14} W cm^{-2}. For all of these reasons, although many concepts valid for high-power lasers can be extended to the X-ray regime, differences in thermal distribution are expected and a simple extrapolation from laser data will not work. In this sense, more efforts are necessary from the theoretical point of view to fully understand the effects of high-intensity X-ray–matter interactions.

Both space and time scales are important in determining the simulation method to numerically approach the problem. Molecular dynamics and Monte Carlo methods (MCs), simulating the motion of atoms, ion and molecules, and the transport of photons and electrons, respectively, are applied in systems with sizes up to the micrometric range for fast processes with a maximum time limit in the picosecond scale (Gnodtke *et al.*, 2009; Neutze *et al.*, 2000; London *et al.*, 2001). As an example, by considering the Seitz–Koehler cross section (Seitz & Turnbull, 1956), which accounts for the atom knock-on by photoelectrons, in a previous study we applied the MC to simulate the displacement of the oxygen doping content to non-active doping positions in $Bi_2Sr_2CaCu_2O_{8+\delta}$ microcrystals. This mechanism was found to be principally responsible for the photoinduced resistivity change for a fraction of the investigated experimental cases (Torsello *et al.*, 2018). For larger scales, once the electrons have thermalized, continuum models are preferred to simulate effects such as melting and cracking (Nicholson *et al.*, 2001; Mino *et al.*, 2017; Wallander & Wallentin, 2017; London *et al.*, 2001). As an example, by means of the finite element method (FEM) we solved the heat equation for an X-ray nanopatterning experiment, calculating the temperature modulation generated by synchrotron pulses (Mino *et al.*, 2017). Similarly, Wallander & Wallentin (2017) modelled the temperature increase induced in an InP nanowire. However, in these cases the derived heating was calculated implementing a heat source implicitly defined as the product between the beam profile and the decaying profile of X-rays as defined by the attenuation-length coefficient, *i.e.* without taking into account the details of the fraction of absorbed photons and of the spatial distribution of the absorbed energy.

In the present work, by continuing our efforts towards the simulation of the heating effects induced by intense X-rays, we want to assess the temperature increase in both space and time in more detail. For this purpose, by considering for the first time both the spatial distribution of the absorbed energy and the real time structure of synchrotron radiation, a more accurate numerical model has been formulated in which the heat source is modulated in both space and time. This was achieved by coupling the radiation-particle transport problem, solved with the MC, with the time-dependent heat equation. With such a detailed model, the temperature increase can be calculated with an unprecedented accuracy. For comparison, the heat equation is also solved implicitly, defining the heat source with the aforementioned method already adopted in the literature.

Table 1
Experimental parameters used for the validation case and the prediction cases.

w and t are the width and the thickness of the samples, while for the bead w refers to the diameter. $\overline{\Phi}_0$ represents the time-averaged photon flux and E_0 is the photon energy. V × H are the horizontal and vertical values of the FWHM of the Gaussian beam profile, as measured by the knife-edge method. V and H were aligned with the x and z axes of the geometrical model.

Sample	w (μm)	t (μm)	$\overline{\Phi}_0$ (photons s^{-1})	E_0 (keV)	V (μm) × H (μm)	Filling mode	Reference
Bead	2000 ± 10%	–	$3.24 \times 10^{12} \pm 15\%$	6.5	84 × 103	–	Snell *et al.* (2007)
WBVB08	6.71	0.38	3.0×10^{11}	17.4	0.050 × 0.070	16 bunch	Mino *et al.* (2017)
WBAP13	13.55	1.6	1.9×10^{11}	17.05	0.117 × 0.116	16 bunch	Pagliero *et al.* (2014)
WBAP14	4.88	1.6	1.0×10^{11}	17.6	0.057 × 0.045	7/8+1	Truccato *et al.* (2016)

In the following, the model validation and accuracy are first discussed by modelling the first thermal-imaging experiment reported in 2006 by Snell *et al.* (Snell *et al.*, 2007). The temperature transient, experimentally monitored by the authors, is compared with that predicted by the model. Then, three examples of X-ray nanopatterning on $Bi_2Sr_2CaCu_2O_{8+\delta}$ microcrystals (Pagliero *et al.*, 2014; Truccato *et al.*, 2016; Mino *et al.*, 2017) are considered to discuss the role of heating on the structural and electrical modifications observed in the fabrication process. For this purpose, the stationary, transient and pulsed regimes of the thermal model are separately treated.

2. Method

2.1. Experimental methods for validation and prediction

Based on their scope, the cases considered can be divided into two categories: validation and prediction. In the validation case, the irradiation of a glass bead (composition in mass percentage: 66% SiO_2, 15% Na_2O, 7% CaO, 5% Al_2O_3, 3% B_2O_3, 2% ZnO, 1% K_2O and 1% MgO) (Snell *et al.*, 2007) at ambient temperature is implemented. In Table 1 the main experimental parameters are summarized. The modelling method used for this case is based on the definition of a range of validity in which the solutions can lie. The range is defined by varying the experimental parameters within their experimental error (reported in Table 1). The complete experimental method can be found in the reference work (Snell *et al.*, 2007). Conversely, the three X-ray nanopatterning experiments fall within the prediction category. In these cases, no experimental measurements of the temperature are given. Therefore, the related simulations have the unique purpose of estimating the temperatures reached during the patterning process. These experiments were directly performed by the authors at the European Synchrotron Radiation Facility (ESRF, Grenoble, France). The experimental details are reported in the following.

To ensure continuity with the previous works, the $Bi_2Sr_2CaCu_2O_{8+\delta}$ samples are named following the same sample nomenclature: WBVB08 (Mino *et al.*, 2017), WBAP13 (Pagliero *et al.*, 2014) and WBAP14 (Truccato *et al.*, 2016). (i) WBVB08 was irradiated at the ID16B beamline using a pink beam ($\Delta E/E \simeq 10^{-2}$) and a 16-bunch filling mode of the storage ring with a maximum current of 90 mA. This filling mode consists of a train of 16 equally spaced highly populated electron bunches, each of them generating a current equal to 90 mA 16-bunch^{-1} = 5.625 mA bunch^{-1} and a Gaussian time profile for the corresponding X-ray pulse with a root mean square (RMS) duration of $RMS_t \simeq 48$ ps. (ii) WBAP13 was irradiated at the ID22 beamline with a monochromatic beam ($\Delta E/E \simeq 10^{-4}$) with 16-bunch filling mode. (iii) WBAP14 was irradiated at the ID16B beamline using a pink beam ($\Delta E/E \simeq 10^{-2}$) with a 7/8+1 filling mode of the storage ring. This mode consists of filling 7/8 of the storage ring length with 868 equally spaced bunches of 0.23 mA per bunch, having at their extremes two bunches of 1 mA. The remaining 1/8 of the storage ring is filled in its centre by a single bunch of 2 mA. This results in a typical RMS duration of the pulses of $RMS_t \simeq$ 20 ps. The samples dimensions are reported in Table 1 together with the experimental beam parameters: time-averaged photon flux $\overline{\Phi}_0$, photon energy E_0 and beam size.

An overview of a typical $Bi_2Sr_2CaCu_2O_{8+\delta}$ chip is reported in Fig. 1(*a*). The irradiated region is located between the voltage electrodes (framed in black) and X-rays perpendicularly impinge on the *ac* plane. As determined during scanning electron microscope (SEM) analysis, this region consists of a section of the $Bi_2Sr_2CaCu_2O_{8+\delta}$ crystal mounted on top of a sapphire substrate (0.5 mm thick) and separated from it by a thin layer of air ∼1 μm in thickness.

2.2. Simulation strategy and geometry

The selection of the simulation method is based on the analysis of the de-excitation processes. The electron relaxation time τ_{el} during which non-thermal phenomena can be observed is less than 1 ps for the systems considered (Lindgren *et al.*, 1999; Truccato *et al.*, 2006; Medvedev, 2015; Kaiser *et al.*, 2000), while the timescale of the heating process is defined by the electron-lattice thermalization $\tau_{el\text{-}ph}$, which is typically a few picoseconds long (Lindgren *et al.*, 1999; Truccato *et al.*, 2006; Gadermaier *et al.*, 2010; Medvedev, 2015; Kaiser *et al.*, 2000). These timescales must be compared with the duration of the X-ray pulse length $t_p \simeq 2.35\ RMS_t$. Synchrotrons have t_p values in the order of tens of picoseconds; therefore, in the first instants of the pulse the sample rapidly reaches the electron-lattice equilibrium and then starts dissipating the absorbed energy by following the thermal route. Accordingly, the spatial dispersion of the absorbed energy within the target, triggered by the emission of photoelectrons and Auger electrons, starts well before the thermal de-excitation process. We have already explored the concept of energy dispersion by means of radiation-transport simula-

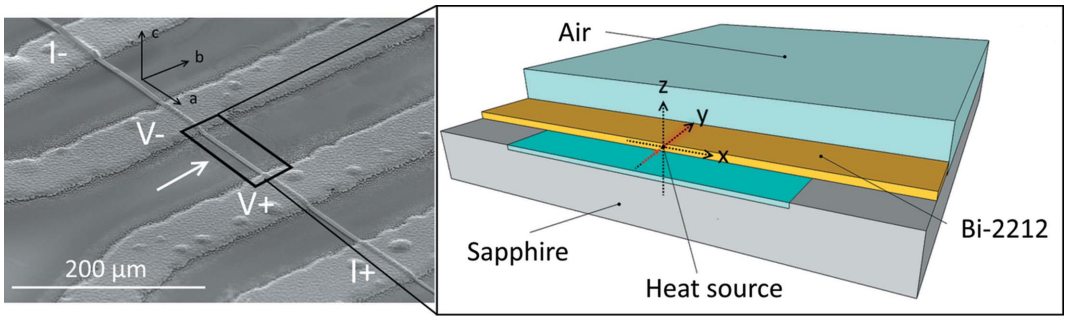

(*a*) (*b*)

Figure 1
(*a*) An SEM micrograph of a typical measurement chip (WBVB08). The current and voltage Ag electrodes are labelled as I+, I− and V+, V−, respectively. The arrow represents the synchrotron nanobeam used for crystal irradiation. (*b*) The 3D model used for the FEM simulations. Sapphire pads under the $Bi_2Sr_2CaCu_2O_{8+\delta}$ crystal represent the regions of strong thermal contact between substrate and crystal. As observed at the SEM, a 1 µm-thick air layer is present under the crystal between these two pads to take into account the poor thermal contact between crystal and substrate. The air layer above the crystal is 100 µm thick (not to scale) and the sapphire substrate is 100 µm thick (not to scale). The red solid arrow indicates the position and direction of the nanobeam. *x*, *y* and *z* axes of the reference frame are oriented along the *a*, *b* and *c* crystallographic axes, respectively.

tions of the X-ray nanopatterning process, finding that the photogenerated electrons exist well beyond the exposed volume and can spread around up to 200 nm from the beam centre (Torsello *et al.*, 2018). Based on these considerations, the fraction of absorbed energy and its spatial distribution, owing to the quick electron-relaxation mechanisms, must be considered to calculate, in an accurate way, the slower and consequent temperature increase. Therefore, the new simulation strategy proposed relies on the coupling of the radiation- and heat-transport physics.

In the present work, when the distribution of the absorbed X-ray energy is considered, it was calculated through the MC using the *MCNP6* code (Goorley *et al.*, 2012) (https://mcnp.lanl.gov/). Each geometry was limited to the region involved in the transport of radiation and particles. Each physical event was tracked by means of a mesh of elementary cubic volumes called voxels. In order to reach a good compromise between space resolution and computation time, the size of voxels edges was fixed to 50 nm.

The heat transport was calculated with the FEM with the software *COMSOL Multiphysics* (Version 4.3b; COMSOL AB, Stockholm, Sweden). The heating source was implemented in agreement with the distribution of energy calculated by means of the radiation-transport simulation. The origin of the frame of reference was set to coincide with the point where the beam strikes the samples. Concerning the geometries, to model the heating of the glass bead, two concentric spheres were used. The inner one represents the glass domain of the bead and the outer one represents the surrounding air domain. The volume of the air domain was fixed to be 20 times the bead radius to safely exclude any influence of the boundary conditions on the results. For the prediction cases, the geometry implemented is more complex and reports only the regions of interest [see Fig. 1(*b*)]. It consists of a 140 µm-long $Bi_2Sr_2CaCu_2O_{8+\delta}$ crystal, representing the crystal portion between the voltage electrodes, surrounded by air (100 µm thick) and by the sapphire substrate (100 µm thick). The silver electrodes were not reported in the models because their distance from the irradiated region (∼70 µm) is large enough not to affect the quality of the results. The thermal contact between crystal and substrate, which is guaranteed in the proximity of the silver electrodes, was represented by means of two sapphire pads located at the extremities of the crystal length [see Fig. 1(*b*)].

2.2.1. *MCNP6* code. In *MCNP6* code, both the photoatomic interactions (photoelectric effect, Compton scattering, coherent and incoherent scattering) and the electron interactions (electron-energy loss, electron angular deflection, Bremsstrahlung emission, Auger electrons, knock-on of electrons) are considered. However, some approximations are made. The crystal structure of the material is not taken into account, so that the materials are always considered as amorphous. Moreover, a low-energy threshold of 1 keV is applied for particle tracking, which neglects the fact that the low-energy particles can move further in space and therefore slightly over-confines energy deposition by the beam in the material.

The photon source was defined specifying the energy of the impinging photon E_0 and the experimental Gaussian profile of the X-ray beam (see Table 1). The latter was approximated by a 2D Gaussian function as follows:

$$I(x, z) = \frac{2}{\pi W_x W_z} \exp\left[-\left(\frac{2x^2}{W_x^2} + \frac{2z^2}{W_z^2}\right)\right], \qquad (1)$$

with W_x and W_z defined as $W_i = \mathrm{FWHM}_i/(2\ln 2)^{1/2} \cong 0.85\,\mathrm{FWHM}_i$, and FWHM_i corresponding to the beam sizes of Table 1.

The deposited energy density for each voxel is expressed per impinging photon $E(x, y, z)$. In order to reach a valid statistical result, the final spatial distribution was calculated with a total number of 10^8 trial photons.

Concerning the photoexcitation conditions, an important difference exists between the validation and the prediction cases. In the former, the ratio between the radial redistribution of the deposited energy (a few hundreds of nm, Fig. S1 in the supporting information), and the micrometric beam size is very small. Therefore, for this case, the contribution of

photoelectrons and secondary electrons is expected to play a minor role in the heating effects. Secondly, because both the beam size and the attenuation length are much smaller than the sample diameter, an important fraction of the volume is not affected by the relaxation phenomena considered in the *MCNP6* code. On the contrary, in the latter cases, along the direction perpendicular to the beam, the spatial length of the energy-redistribution processes is comparable with the nanometric dimension of the spot size. This is represented in Fig. 2, in which the energy-density distribution for the prediction cases WBVB08, WBAP13 and WBAP14 is reported as a function of the beam penetration direction y and of the two perpendicular directions z [Figs. 2(*a*), 2(*b*) and 2(*c*)] and x [Figs. 2(*d*), 2(*e*) and 2(*f*)], respectively. The effects of energy dissipation are evident in the distribution widths, which are wider than the corresponding FWHM of the beam profile. Nonetheless, the energy-density distributions are still correlated with the beam shape. This is highlighted by the fact that the lateral spread of the energy densities rescales coherently with the X-ray beam size adopted in each experiment. Finally, on the beam direction, a fraction of the incident energy is transmitted. From these calculations, it is visible how, in these cases, an accurate definition of the energy distribution becomes important.

In Table 2 the peak values of the energy-density distributions (E_{max}) are summarized for each sample.

2.2.2. *COMSOL* model. Since t_p is much greater than both τ_e and $\tau_{el\text{-}ph}$, the classical Fourier heat diffusion equation should provide a good description of the temperature evolution. The Fourier heat equation is then used:

$$\rho C_p \frac{\partial T}{\partial t} + \nabla \cdot (-k \nabla T) = Q, \qquad (2)$$

Table 2
Maximum energy values E_{max} derived from the MC simulations reported in Fig. 2, and the corresponding maximum power-density values $\overline{P}_{ex\,max} = \overline{\Phi}_0 E_{max}$.

The maximum of the power density for the implicit case $\overline{P}_{im\,max}$ is also reported. The E_{max} value of the validation case of Fig. S1 is also shown.

Sample	E_{max} (J m^{-3})	$\overline{P}_{ex\,max}$ (W m^{-3})	$\overline{P}_{im\,max}$ (W m^{-3})
Bead	1.470×10^{-3}	4.8×10^{9}	6.7×10^{9}
WBVB08	2920	8.8×10^{14}	1.2×10^{16}
WBAP13	1140	2.2×10^{14}	1.9×10^{15}
WBAP14	3500	3.5×10^{14}	5.6×10^{15}

where T represents the space- and time-dependent temperature field, ρ, C_p and k are the density, the heat capacity at constant pressure and the thermal conductivity of the materials (see values listed in Table 3), respectively, and Q represents the heat source. The thermal coefficients of the materials were created to be constant in the temperature range of interest. Boundary conditions were assumed by imposing a constant temperature, equal to the ambient temperature, on all the model external boundaries.

In the explicit case, the heat source Q of the FEM model was set equal to the power density absorbed by the crystal $P_{abs\,ex}$,

$$Q_{ex}(x, y, z, t) = P_{abs\,ex}(x, y, z, t) = \Phi(t)\, E(x, y, z), \qquad (3)$$

with $\Phi(t)$ representing the instantaneous photon flux and $E(x, y, z)$ representing the deposited energy-density distribution as calculated by MC simulations. Moreover, in order to highlight the impact of the MC simulation in the X-ray heating process, the same model was also solved ignoring the physics of the beam–crystal interaction. In this case, the space distribution of the heating power Q was implicitly considered equal to the space distribution of the X-ray absorption, as appears

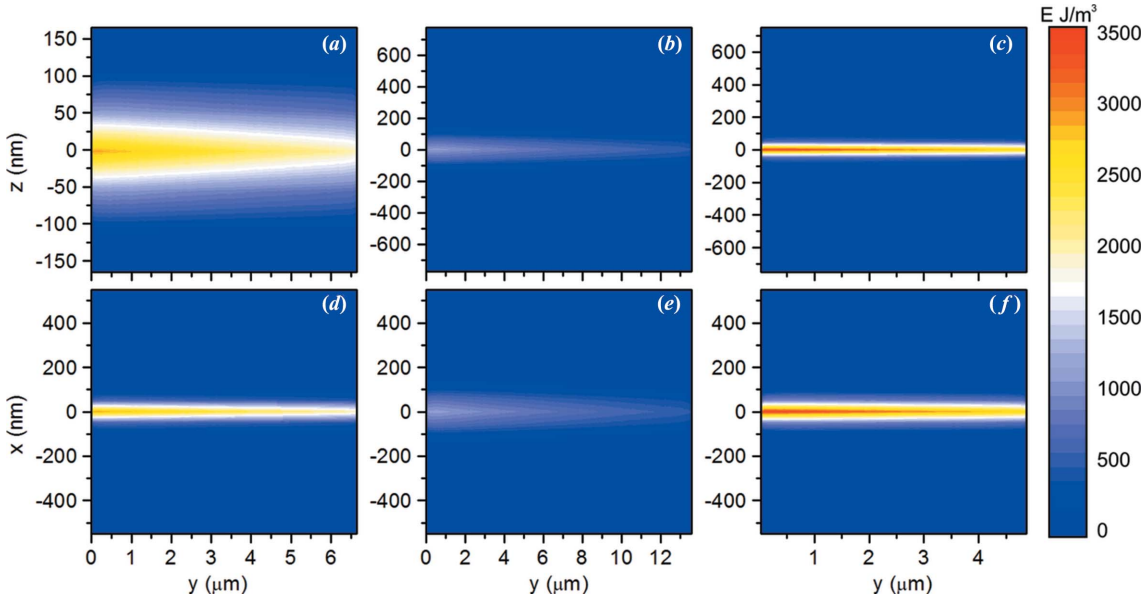

Figure 2
2D plots of the energy spatial distributions evaluated by the *MCNP6* code. For samples WBVB08, WBAP13 and WABAP14, (*a*), (*b*) and (*c*) show the *zy* cross sections ($x = 0$) of the model, corresponding to the *bc* plane of the crystals (the z direction is aligned with sample thickness), and (*d*), (*e*) and (*f*) show the *xy* cross sections ($z = 0$), corresponding to the *ab* plane of the crystals.

Table 3
Thermodynamic properties of materials at ambient temperature used in the model.

Material	ρ (kg m^{-3})	C_p (J kg^{-1} K^{-1})	k (W m^{-1} K^{-1})
Glass bead	2500 (Snell *et al.*, 2007)	799 (Snell *et al.*, 2007)	0.97 (Snell *et al.*, 2007)
$Bi_2Sr_2CaCu_2O_{8+\delta}$	6700 (Subramanian *et al.*, 1988)	450 (Natividad *et al.*, 2006)	0.88 (*c* plane), 6.29 (*ab* axis) (Crommie & Zettl, 1990)
Sapphire	4000 (Burghartz & Schulz, 1994)	780 (Archer, 1993)	40 (Burghartz & Schulz, 1994)
Air	1.2 (US standard atmosphere, 1976)	1012 (Lide, 2003)	0.026 (Lide, 2003)

from the experimental conditions. Therefore, along the beam direction (*i.e.* the *y* axis) the power absorbed was represented in agreement with the Lambert–Beer law, and along the two directions normal to the beam direction it was defined by means of the experimental intensity profile of the incident beam [equation (1)]. The final form of the implicit definition of the heat source is equal to

$$Q_{\rm im}(x,y,z,t) = P_{\rm abs\,im}(x,y,z,t) = \frac{2\Phi(t)E_0}{\pi W_x W_z \lambda}\exp\left[-\left(\frac{y}{\lambda}+\frac{2x^2}{W_x^2}+\frac{2z^2}{W_z^2}\right)\right], \quad (4)$$

where λ represents the attenuation length of the material [51 µm for glass and ∼17 µm for $Bi_2Sr_2CaCu_2O_{8+\delta}$ (Henke *et al.*, 1993)]. For simplicity, in the following we will refer to the two approaches, resulting from the use of the two heat sources $Q_{\rm ex}$ and $Q_{\rm im}$, as the explicit and implicit methods, respectively.

By substituting the instantaneous photon flux $\Phi(t)$ with the experimental time-averaged photon flux $\overline{\Phi}_0$ (see Table 1), the total time-averaged power density absorbed by the samples was obtained. In Table 2, with $\overline{P}_{\rm im\,max}$ and $\overline{P}_{\rm ex\,max}$ the corresponding maximum values are reported for the implicit and explicit methods, respectively.

A few hundreds of thousands of elements were created in the mesh, and a computer with 88 Gb of RAM and two processors with a clock of 2.4 GHz were used for the calculations. The computing time for all the simulations did not exceed 12 h.

3. Results and discussion

3.1. Validation case

We have carried out the simulation corresponding to the validation case by calculating the transient behaviour induced in the experimental conditions in the work of Snell *et al.* (2007) in the presence of a time-averaged photon flux $\overline{\Phi}_0 = 3.24 \times 10^{12}$ photons s^{-1} (see Table 1). In Fig. 3, the evolution of the experimental (dots) and the calculated (lines) heating for the glass bead is reported within the first 5 s of irradiation. The data refer to the average temperature at the sample surface in the area impinged by the beam. The solid lines define the limits of the range (highlighted in grey) of all of the possible behaviours predicted with the explicit method. The upper and lower limits were found by considering the experimental ranges shown in Table 1. A good agreement between experimental and calculated behaviours is shown. Indeed, except for the first instants of irradiation, the experimental data fall inside the simulated range. It is also important to note that if other experimental uncertainties were implemented, the range of existence of the simulated behaviour (which was found considering only the variations in the sphere diameter and in the photon flux) would be even wider. Among the uncertainties, the geometry and materials of the sphere holder, the shape irregularities present in the sample geometry, and the imperfect alignment of the beam direction with the centre of the bead would certainly play a role in further increasing the grey area of Fig. 3. This means that to have an accurate prediction of the X-ray heating, all the experimental parameters must be carefully controlled and the experimental uncertainties minimized.

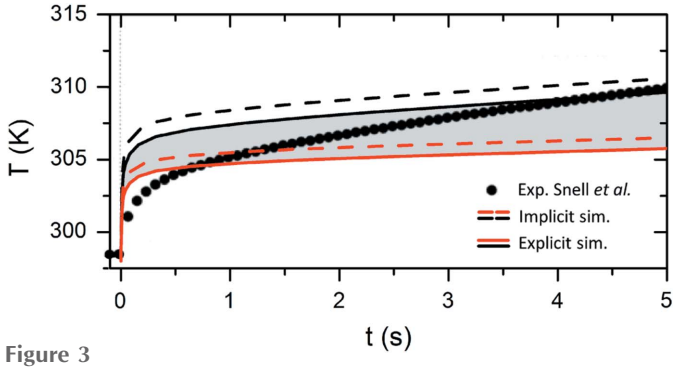

Figure 3
Comparison between the experimental (dots) and the simulation results (lines) for the validation case of the bead. The dashed and the solid lines represent the simulations with the implicit and the explicit definition of the heating source, respectively. The red lines correspond to the heating induced by the lowest photon-flux density and the biggest bead radius compatible with the experimental error reported. The black lines correspond to the case with the highest photon-flux density and the smallest bead radius compatible with the experimental error. The experimental data have been digitalized from Snell *et al.* (2007).

In Fig. 2, the theoretical behaviour predicted by the implicit method is also reported with the dashed lines. As expected, the heating for the implicit method is slightly greater than the one calculated with the explicit method. However, this is coherent with the fact that the ratio between the nanometric length of the diffusive behaviour of the relaxation phenomena and the micrometric dimension of the X-ray beam is very small.

3.2. Prediction cases

3.2.1. Steady-state solution. The steady-state solution of the model can be easily obtained by imposing a vanishing time derivative in equation (2) and assuming that the heat source is time independent, then $\Phi(t) = \overline{\Phi}_0$. The corresponding temperature distributions obtained defining the heat source with the explicit method are shown in Fig. 4 for the samples

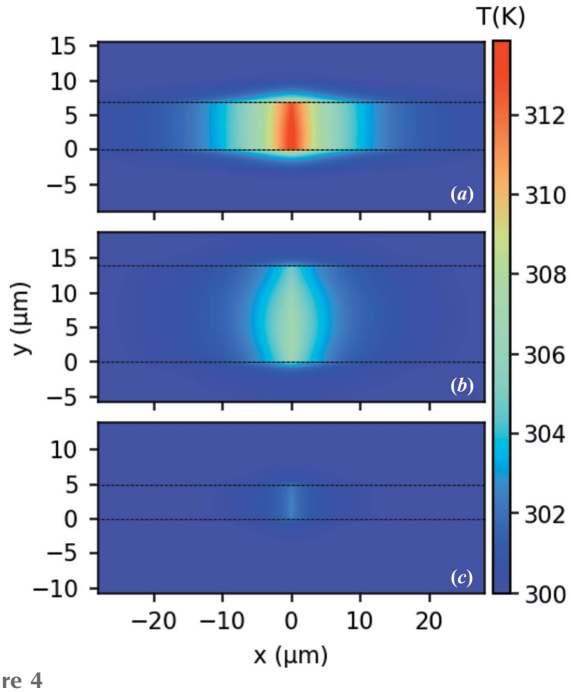

Figure 4
Calculated temperature spatial distribution induced in the crystals during irradiation in hypothetical steady-state conditions for samples (*a*) WBVB08, (*b*) WBAP13 and (*c*) WBAP14. The cross-section plane is located at half thickness of the crystal. The nanobeam axis lies in the plane and is aligned along the *y* direction, with the point (x = 0 μm, y = 0 μm) representing its incidence point on the crystal.

WBVB08 [Fig. 4(*a*)], WBAP13 [Fig. 4(*b*)] and WBAP14 [Fig. 4(*c*)]. It can be observed that the temperature increase is significant only within ∼30 μm from the beam, which confirms *a posteriori* the possibility of safely neglecting in the model the presence of the Ag contacts. Furthermore, air heating can be appreciated only within a maximum distance of ∼3 μm from the crystal surface. Therefore, the confinement of the temperature increase in these regions also confirms the validity of the boundary conditions assumed for the model. The maximum temperature T_{max} is ∼314, 307 and 303 K for the samples WBVB08, WBAP13 and WBAP14, respectively.

This is in accordance with the fact that sample WBVB08 is the one with the highest maximum value $\overline{P}_{ex\,max}$. However, this seems to be not the only parameter that determines T_{max}. Indeed, although $\overline{P}_{ex\,max}$ has the lowest intensity in WBAP13, the temperature rise calculated in this case is not the lowest one. This indicates that T_{max} is also strongly dependent on the energy spatial distribution of the heating source.

Figs. 5(*a*), 5(*b*) and 5(*c*) display the corresponding temperature profiles calculated inside the crystals along the beam direction for samples WBVB08, WBAP13 and WBAP14, respectively. A temperature decrease can be noticed near the incident surface owing to the cooling effect of air. In this regard, measuring the distance dT_{max} between the incidence surface and the position of T_{max} and normalizing it with respect to the crystal width w, a linear correlation is found with T_{max} [Fig. 5(*d*)]. This implies that the higher the

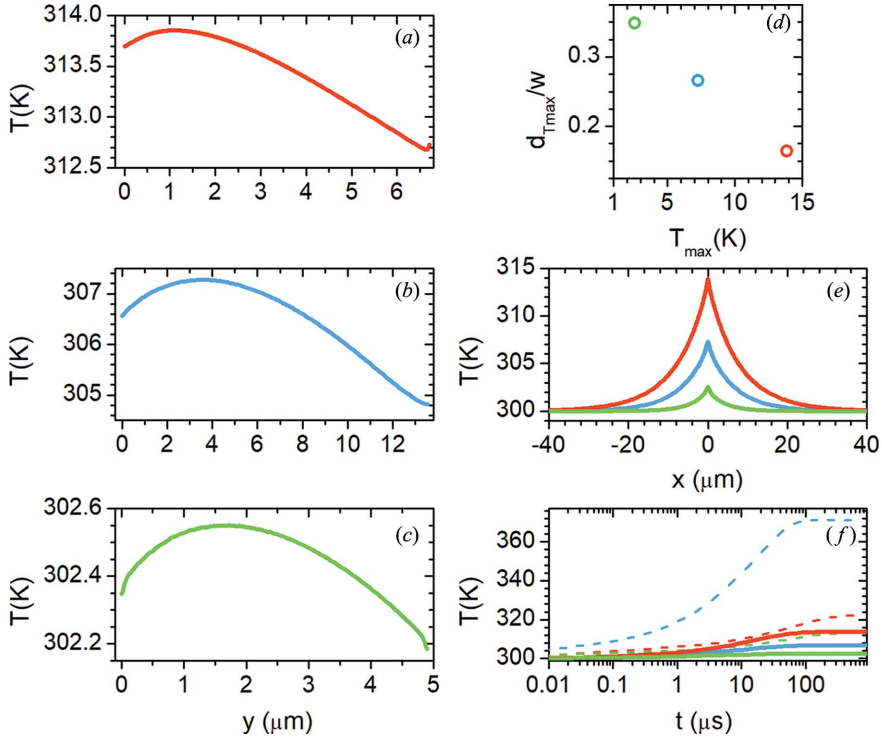

Figure 5
Spatial distribution of the temperature during irradiation in steady-state conditions according to the explicit method (MC + FEM simulations). Left panels show the temperature profile along the beam axis: (*a*) red line for WBVB08, (*b*) blue line for WBAP13 and (*c*) green line for WBAP14. With the same colours in the right panels: (*d*) the linear correlation between the normalized distance of the T_{max} point as a function of the temperature increase, (*e*) the temperature distribution along the length of the crystals plotted along a line parallel to the *x* axis crossing the hottest point, and (*f*) the temperature temporal evolution at the T_{max} point as calculated by FEM with (solid lines) and without (dashed lines) MC simulations. At t = 0 the irradiation starts, and the logarithmic scale has been used to highlight the different times at which temperatures saturate.

temperature, the closer (in relative units dT_{max}/w) the T_{max} point will be to the X-ray incidence surface. The temperature behaviours in the crystal-length direction (x axis of the model) are reported in Fig. 5(e) for samples WBVB08, WBAP13 and WBAP14 in red, blue and green lines, respectively. The temperature profiles decay to room temperature less rapidly with the increase of T_{max}. Moreover, at most 40 µm away from the incidence point all the samples reach the ambient temperature, confirming the confinement of the heating effect.

3.2.2. Transient solution. The evolution of the temperature in the crystals under transient conditions, *e.g.* after turning the beam on at $t = 0$, can be studied by restoring the time-derivative term in equation (2), while keeping the heat-source term Q equal to a time-independent constant $\overline{Q}$. The corresponding time behaviours shown in Fig. 5(f) for samples WBVB08, WBAP13 and WBAP14 calculated at the hottest point are represented with the solid red, blue and green curves, respectively. In the same figure, with the same colours, the corresponding behaviours calculated with the implicit method are represented with dashed lines. In general, three regimes can be distinguished: (i) an initial very fast increase of the temperature (typically less than a few microseconds), (ii) a slowdown of the heating rate and (iii) a final steady-state condition. Comparing the results from the implicit and the explicit models, the overestimation of the heating response obtained with the former method is clear.

3.2.3. Time-dependent solution. The implementation of the model with the pulsed nature of synchrotron radiation adds a remarkable complication to the problem by concentrating the absorbed power density in time intervals of tens of picoseconds and by modulating the pulse features in frequency and intensity. In order to obtain a closer description of the experimental situation, the real-time dependence of the heat-source term, $Q = Q(t)$, was implemented in the model. The single time pulse of the beam is Gaussian in shape and has an RMS duration RMS_t defined according to the relation $\mathrm{FWHM}_t \cong 2.35\ \mathrm{RMS}_t$. Therefore, in both equations (3) and (4), $\Phi(t)$ can be rewritten for each pulse as

$$\Phi(t) = \Phi_0(t_{0,i}) \exp\left\{-\left[\frac{2(t - t_{0,i})^2}{W_t^2}\right]\right\},$$

where $W_t = \mathrm{FWHM}_t/(2\ln 2)^{1/2} \cong 0.85\,\mathrm{FWHM}_t \cong 1.996\,\mathrm{RMS}_t$ represents the pulse duration, $t_{0,i}$ represents the time of the ith peak pulse, and $\Phi_0(t_{0,i})$ is the corresponding instantaneous photon flux. Since the time pattern of the beam flux is periodically repeated with a period $T_{rev} = 2.82$ µs, $\Phi_0(t_{0,i})$ can be determined for each mode of the storage ring by requesting that

$$\int_{t}^{t+T_{rev}} \Phi_0(t')\,dt' = \overline{\Phi}_0 T_{rev}. \qquad (5)$$

The values of the parameters used to describe the time modulation of the synchrotron radiation are listed in Table 4.

In 16-bunch filling mode, used for samples WBVB08 and WBAP13, all of the pulses are equal and $\Phi_0(t_{0,i}) = \overline{\Phi}_0 T_{rev}/[16 W_t (\pi/2)^{1/2}]$. Fig. 6($a$) shows the time behaviour of the power density at the beam incidence point $Q(0, t)$ corresponding to the first eight bunches, normalized to their peak value Q_{tmax} which corresponds to the most intense power density at the incidence point obtained at $t_{0,i}$, *i.e.* when the absolute maximum flux $\Phi_0(t_{0,i})$ is reached. On the other hand, in the 7/8+1 mode (sample WBAP14) three different kinds of pulses are present, with intensities of 0.23, 1 and 2 mA bunch^{-1}. The instantaneous flux corresponding to the smallest peak can be obtained from equation (5) as $\Phi_0(t_{0,i}) = 0.23\overline{\Phi}_0 T_{rev}/[203.64 W_t (\pi/2)^{1/2}]$. The time evolution of the normalized power density $Q(0, t)/Q_{tmax}$ for sample WBAP14 is represented in Fig. 6(b) for two representative portions of the time pattern.

16-bunch irradiation of WBVB08 and WBAP13. The comparison between the temperature time behaviours of the transient and the time-dependent solutions, as calculated at the hottest point with the explicit method, is reported in Fig. 7(a) for WBVB08 and in Fig. 7(b) for WBAP13. Because of the dense time packing of the X-ray energy, the temperature rapidly increases in correspondence with the pulse arrival. Indeed, the instantaneous heating power density is four orders of magnitude larger than the respective steady-state cases. In the first pulse, the temperature rises to a maximum of ∼340 and 312 K within ∼350 ps in samples WBVB08 and WBAP13, respectively. Then, it slowly decreases in the interval between two pulses, reaching a minimum temperature of ∼300 K immediately before the second pulse arrives. In Figs. 7(a) and 7(b), it is also possible to appreciate how the difference

Table 4
Parameters used to determine the peak power density at the beam incidence point for the case of the pulsed heat source.

For the 7/8+1 mode, three values are indicated for $\Phi_0(t_{0,i})$, corresponding to the three different types of peaks contained in the 7/8+1 filling pattern.

Sample	Mode	RMS_t (ps)	FWHM_t (ps)	W_t (ps)	$\Phi_0(t_{0,i})$ (10^{13} photons s^{-1})
WBVB08 WBAP13	16 bunch	48	112.8	95.88	43.84 27.77
WBAP14	7/8+1	20	47	39.95	0.63 2.76 5.51

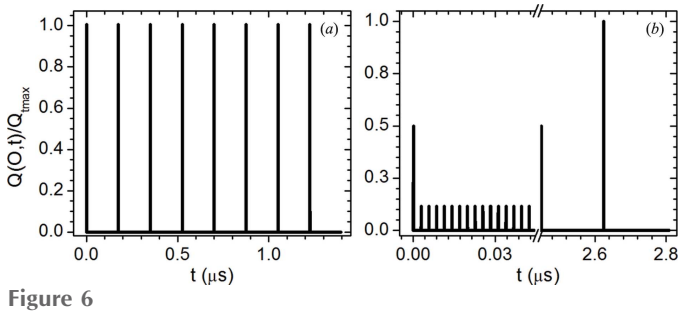

Figure 6
Temporal evolution of the normalized power density $Q(0, t)/Q_{tmax}$ for the two filling modes of the storage ring: (a) 16-bunch mode, corresponding to irradiation of samples WBVB08 and WBAP13 (only the first eight bunches after $t = 0$ are shown), and (b) 7/8+1 mode, corresponding to irradiation of sample WBAP14 (different portions of the period are shown).

between the transient (red and blue curves) and the pulsed solutions (corresponding black curves) becomes more evident with increasing the maximum temperature achieved with the pulsed heat source. This fact clarifies how considering synchrotron experiment's measurements and simulations, that average the sample temperature over time scales of the order of 100 ns or more, can result in an underestimation of the real instantaneous sample temperature.

In Figs. 7(*d*) and 7(*e*), a blow-up of the first temperature peak, as calculated with the explicit (solid line) and implicit (dashed lines) methods, is reported for samples WBVB08 and WBAP13, respectively. It is possible to observe that the temperature increases simulated with the implicit method are about one order of magnitude higher than those obtained with the explicit method. Precisely, an overestimation of ∼500 and 90 K for the samples WBVB08 and WBVB13 is obtained with the implicit method, respectively. By comparing these results with those shown in Fig. 5(*f*), for the corresponding transient cases, it can be observed how the temperature difference between the implicit and explicit methods becomes larger when the time modulation of the heat source is considered.

7/8+1 irradiation of WBAP14. The heating evolution calculated with the explicit method at the maximum temperature point of WBAP14 is reported in Fig. 7(*c*). The more complex structure of the irradiation time pattern is reflected in the temperature evolution of the sample: the two temperature peaks of ∼301.5 and 303 K (at $t \simeq 0$ and $t \simeq 2500$ ns, respectively), corresponding to the two 1 mA bunches of the storage ring, delimit the train of 868 smaller bunches, generating lower temperature peaks whose maxima lie between 300 and 301 K. The highest temperature peak at ∼304 K corresponds to the single bunch of 2 mA (at $t \simeq 2600$ ns). It can be noted that the temperature increase is lower than in the cases in 16-bunch mode. This is consistent with the peak value of the heat source of 1.9×10^{17} W m^{-3} (2 mA pulse), which is considerably less than those calculated for samples WBVB08 and WBAP13 of 1.3×10^{18} W m^{-3} and 3.2×10^{17} W m^{-3}, respectively. By comparing the time-dependent solution with the transient solution (green line), it can be noted that in the region of the closely spaced pulses at $t \simeq 0$ ns the first three peaks have a minimum temperature which is higher than the transient behaviour. This is caused by the presence of the 1 mA peak at $t \simeq 0$ in the power density $Q(t)$. Indeed, after the repetition of the 868 pulses, the temperature of the transient case is stabilized and the baseline of the pulsed profile falls below the transient behaviour as expected, because the transient solution should represent a sort of time average of the real pulsed regime. A maximum difference of ∼2 K from the transient behaviour can be detected in this region around $t \simeq 2440$–2800 ns for the last two pulses.

In Fig. 7(*f*), the temperature evolution calculated from the explicit method is compared with the one derived from the implicit method for the most intense peaks observed in sample WBAP14. A maximum overestimation of the heating of ∼40 K is obtained. Therefore, the lower heating predicted with the explicit method can be considered as an improvement in the accuracy of the model. This fact not only clarifies the role of the absorbed-energy spatial distribution in the thermal phenomenon but it also allows us to effectively determine the impact of the thermal effects in the observed-material property changes. From this point of view, the hypothesis that very high temperature peaks could have been induced by X-rays during these experiments must be rejected. Anyway, the possibility that synchrotron pulses may induce thermal stresses in the crystals cannot be excluded. Indeed, plastic deformation and cracks formation can occur because of the strong thermal gradient (Moshe *et al.*, 2000; Nicholson *et al.*, 2001; Hau-Riege, 2012). Moreover, even in the case that thermal and mechanical phenomena are not important, the repetitive pulsed irradiation can cause thermal fatigue and fracture (de Castro *et al.*, 2010; Ryutov, 2003). The numerical assessment of these possibilities requires more dedicated investigations.

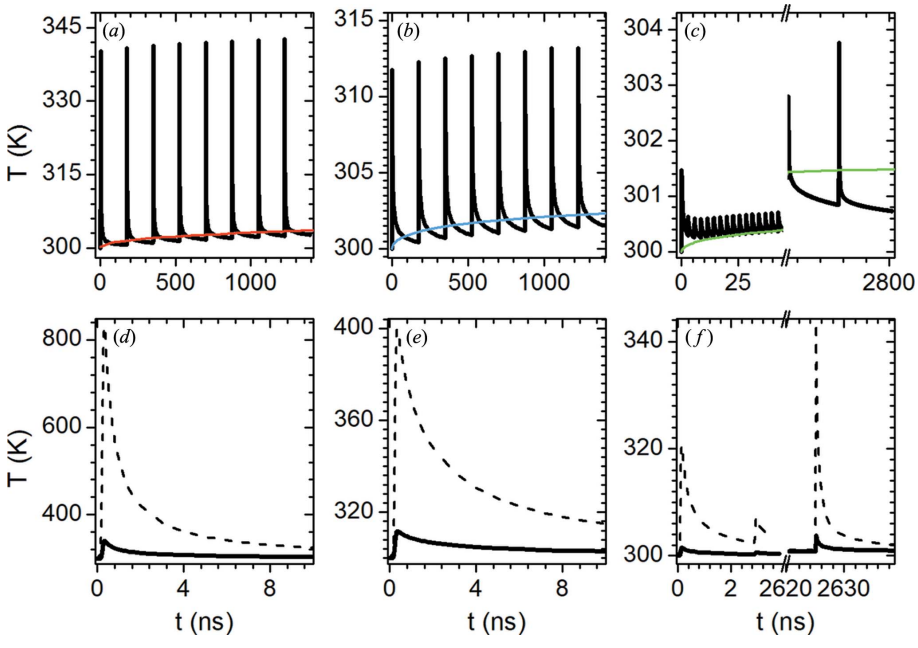

Figure 7
Simulation of the X-ray-induced heating calculated at the point of maximum temperature by considering the time pattern of the source. The predictions obtained with the explicit method for samples WBVB08, WBAP13 and WBAP14 are shown in (*a*), (*b*) and (*c*), respectively. Black lines represent the time-dependent studies and coloured lines show the corresponding transient behaviour in steady-state conditions, already shown in Fig. 5(*e*). Following the same sample order, in (*d*), (*e*) and (*f*) the corresponding simulations are compared with the those calculated with the implicit method (dashed lines).

The temperature distributions calculated at the instant of maximum temperature increase with the explicit method are reported in Fig. 8. For all of

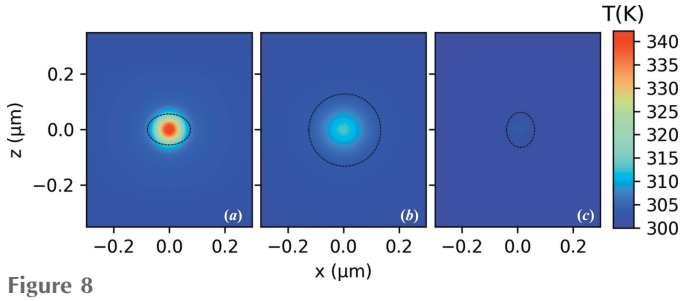

Figure 8
Calculated temperature spatial distribution induced by the nanobeams in the pulsed regime as calculated with the explicit method for samples WBVB08 (*a*), WBAP13 (*b*) and WBAP14 (*c*). The *xz* cross-section planes pass across the hottest points and correspond to the instant of maximum temperature reached by each sample. Black contour lines indicate the half-maximum intensity points of the incident beam.

the samples, the heating effects are almost completely confined within the beam spot size.

3.2.4. Adiabatic approximation. It is important to note that without considering the photoatomic interactions and the electron interactions, it is not possible to correctly estimate the instantaneous temperature increase for the experiments. On the contrary, if the spatial extension of these interaction is given by any simulation code, it is possible to exploit the adiabatic approximation to obtain a preliminary estimation of the results of the numerical solution of the heat-transfer equation. Indeed, if we consider the predictive cases corresponding to the $Bi_2Sr_2CaCu_2O_{8+\delta}$ X-ray nanopatterning experiments, the thermal diffusivity of the material is given by $\alpha = k_{ab}/\rho C_p = 2.09 \times 10^{-6}\ m^2\ s^{-1}$. This implies that for any typical radius Δr of the cylindrical volume where energy deposition takes place around the beam axis, the time Δt needed by the heat to diffuse out of this region is of the order of $\Delta r^2/\alpha$. It can be easily checked, even in the case of a very small Δr value in the order of magnitude of 100 nm, then $\Delta t \simeq$ 4.8 ns, which is much longer than any X-ray pulse duration reproduced by our numerical simulations (20–50 ps). This means that the energy deposition is so fast that during each pulse there is no time for the heat to diffuse out of the energy-deposition region, which makes the adiabatic approach meaningful. Therefore, during such a short timescale, the energy-deposition volume can be considered as isolated from the rest of the sample and the corresponding temperature increase can be calculated, which is expected to correspond to the maximum temperature reached in the sample.

Therefore, the definition of the energy-deposition volume is an important step. Because of the irradiation geometry, this volume can be identified with a cylindrical volume with radius Δr and height Δl. Keeping in mind that we are interested in estimating the maximum temperature to be observed in the sample, it is expected that the point where this temperature is reached has to be close to the sample surface, which means that this point lies in the sample within a depth that is much less than the X-ray attenuation depth λ. Therefore, the choice $\Delta l = \lambda/10$ is expected both to contain the maximum temperature point and to be reasonably uniform in energy deposition and in temperature increase. Concerning the radius

Table 5
Parameters used to estimate the instantaneous maximum temperature ΔT at the peak photon flux in adiabatic approximation.

λ represents the X-ray attenuation depth, $FWHM_{xz}$ refers to the transverse Gaussian profile of the energy deposition and E_{bunch} is the energy of all of the photons of a single bunch.

Sample	λ (μm)	$FWHM_{xz}$ (nm)	E_{bunch} (pJ)	ΔT (K)
WBVB08	17.8	263	147	48.3
WBAP13	16.9	520	91.4	8.03
WBAP14 (smallest peaks)	18.3	470	3.9	0.39

Δr, this can be estimated only on the basis of the MC results. By fitting to Gaussian curves (see supporting information) the cross-section profiles of the energy-deposition curves plotted in Fig. 2, the $FWHM_{xz}$ values reported in Table 5 can be obtained.

Therefore, a natural choice in this respect involves assuming $\Delta r = FWHM_{xz}/2$. Then, the maximum temperature increase ΔT can be estimated by considering all of the energy absorbed by the cylinder during a single bunch as heat adiabatically delivered to it,

$$\Delta T = \frac{E_{bunch}[1 - \exp(-0.1)]}{mC_p},$$

where E_{bunch} is the energy corresponding to all of the photons of a single bunch, and $m = \rho\pi\Delta r^2\Delta l$. The corresponding values are listed in Table 5 and compare reasonably well with the results from the numerical solutions.

4. Conclusions

In this work, the Fourier heat equation was solved with the finite element method to simulate the X-ray heating effects induced by third-generation synchrotrons in inorganic materials. Two approaches were used to define the heat-source term. In addition to the already reported approach, in which the heat source is implicitly approximated by using the experimental parameters coming from the beam profile and the material attenuation length, we proposed a second method in which the heat source is defined explicitly. This is carried out using the Monte Carlo method which explicitly considers the photon and particle interactions involved in the absorption and relaxation processes of the target. Both of the models were applied to simulate the heating measurements carried out by Snell *et al.* (2007) in a millimetric glass bead, finding a good agreement. However, it also emerges how a control of the experimental parameter is fundamental to accurately model the system and reduce the variation of the predicted behaviour.

In the other scenario explored, the role of heating in three examples of X-ray nanopatterning experiments, performed in $Bi_2Sr_2CaCu_2O_{8+\delta}$ microcrystals (Mino *et al.*, 2017; Pagliero *et al.*, 2014; Truccato *et al.*, 2016), was predicted. For these cases, the theoretical prediction of the heating behaviours was studied modelling the heat source in stationary and time-

dependent conditions, *i.e.* the filling pattern of the storage ring was considered when modulating in time the heat source.

In the stationary case, the maximum temperature achieved is found to be dependent not only on the power density but also on the spatial distribution of the heat source in the plane normal to the beam. Moreover, an overestimation of up to tens of degrees is obtained with the implicit method. This strong difference was attributed to the energy redistribution that takes place because of photoelectron emission and transport. This implies that the more accurate definition of the power-density distribution in the explicit method is fundamental when X-ray nanobeams are considered, *i.e.* when the irradiated region is in the same order of the diffusion length of the photoelectrons. In the time-dependent problem, in which the pulsed behaviour of synchrotrons is considered, the heating phenomenon was demonstrated to be roughly proportional to the instantaneous peak value of the absorbed power density. Finally, in this more complex regime, the comparison between the implicit and explicit methods highlighted the crucial impact of the power-density distributions. Indeed, in the implicit method, which disregards the energy distribution taking place with photoabsorption events, an overestimation of the thermal effects of the order of hundreds of degrees is predicted. Conversely, if the spatial redistribution of the absorbed energy is explicitly considered, an adiabatic approach can estimate the temperature increase reasonably well.

Ultimately, from the point of view of the X-ray nanopatterning process, the calculated instantaneous temperature increase, for the three considered samples, varies from a few degrees to tens of degrees. Therefore, by considering that $Bi_2Sr_2CaCu_2O_{8+\delta}$ has a melting temperature of $\sim$860°C, an ordinary melting process can be excluded.

Acknowledgements

The authors thank the ESRF for the beam time allocated.

Funding information

MT and VB acknowledge partial support from the 'Department of Excellence' (L.232/2016) grant, funded by the Italian Ministry of Education, University and Research (MIUR). This work has been partly carried out under project NANO-X, jointly approved and funded by University of Turin and Compagnia di San Paolo.

References

Adriaens, A., Quinn, P., Nikitenko, S. & Dowsett, M. G. (2013). *Anal. Chem.* **85**, 9556–9563.
Archer, D. G. (1993). *J. Phys. Chem. Ref. Data*, **22**, 1441–1453.
Bahk, S. W., Rousseau, P., Planchon, T. A., Chvykov, V., Kalintchenko, G., Maksimchuk, A., Mourou, G. A. & Yanovsky, V. (2004). *Opt. Lett.* **29**, 2837–2839.
Bonino, V., Agostino, A., Prestipino, C., Hernandez, O., Fretto, M., Mino, L. & Truccato, M. (2018). *CrystEngComm*, **20**, 6667–6676.
Bonino, V., Mino, L., Agostino, A., Prestipino, C., Fretto, M. & Truccato, M. (2019). *Proc. SPIE*, **11035**, 110350I.
Bras, W. & Stanley, H. (2016). *J. Non-Cryst. Solids*, **451**, 153–160.
Burghartz, S. & Schulz, B. (1994). *J. Nucl. Mater.* **212–215**, 1065–1068.
Castro, A. R. B. de, Vasconcellos, A. R. & Luzzi, R. (2010). *Rev. Sci. Instrum.* **81**, 073102.
Crommie, M. F. & Zettl, A. (1990). *Phys. Rev. B*, **41**, 10978–10982.
Feldman, Y., Lyahovitskaya, V., Leitus, G., Lubomirsky, I., Wachtel, E., Bushuev, V. A., Vaughan, G., Barkay, Z. & Rosenberg, Y. (2009). *Appl. Phys. Lett.* **95**, 051919.
Gadermaier, C., Alexandrov, A. S., Kabanov, V. V., Kusar, P., Mertelj, T., Yao, X., Manzoni, C., Brida, D., Cerullo, G. & Mihailovic, D. (2010). *Phys. Rev. Lett.* **105**, 257001.
Gnodtke, C., Saalmann, U. & Rost, J. M. (2009). *Phys. Rev. A*, **79**, 041201.
Goorley, T., James, M., Booth, T., Brown, F., Bull, J., Cox, J., Durkee, J., Elson, J., Fensin, M., Forster, R. A., Hendricks, J., Hughes, H. G., Johns, R., Kiedrowski, B., Martz, R., Mashnik, S., McKinney, G., Pelowitz, D., Prael, R., Sweezy, J., Waters, L., Wilcox, T. & Zukaitis, T. (2012). *Nucl. Technol.* **180**, 298–315.
Hau-Riege, S. P. (2012). *High-Intensity X-rays – Interaction with Matter: Processes in Plasmas, Clusters, Molecules and Solids.* Hoboken, New Jersey: Wiley.
Henke, B. L. G. E. M., Gullikson, E. M. & Davis, J. C. (1993). *At. Data Nucl. Data Tables*, **54**, 181–342.
Hsu, P.-C., Chen, Y.-S., Hwu, Y., Je, J. H., Margaritondo, G. & Tok, E. S. (2015). *J. Synchrotron Rad.* **22**, 1524–1527.
Kaiser, A., Rethfeld, B., Vicanek, M. & Simon, G. (2000). *Phys. Rev. B*, **61**, 11437–11450.
Lide, D. R. (2003). *CRC Handbook of Chemistry and Physics.* CRC Press: Boca Raton.
Lindgren, M., Currie, M., Williams, C., Hsiang, T. Y., Fauchet, P. M., Sobolewski, R., Moffat, S. H., Hughes, R. A., Preston, J. S. & Hegmann, F. A. (1999). *Appl. Phys. Lett.* **74**, 853–855.
Liu, X., Du, D. & Mourou, G. (1997). *IEEE J. Quantum Electron.* **33**, 1706–1716.
London, R. A., Bionta, R. M., Tatchyn, R. O. & Roesler, S. (2001). *Proc. SPIE*, **4500**, 51–62.
Martínez-Criado, G., Villanova, J., Tucoulou, R., Salomon, D., Suuronen, J.-P., Labouré, S., Guilloud, C., Valls, V., Barrett, R., Gagliardini, E., Dabin, Y., Baker, R., Bohic, S., Cohen, C. & Morse, J. (2016). *J. Synchrotron Rad.* **23**, 344–352.
Martis, V., Nikitenko, S., Sen, S., Sankar, G., van Beek, W., Filinchuk, Y., Snigireva, I. & Bras, W. (2011). *Cryst. Growth Des.* **11**, 2858–2865.
Medvedev, N. (2015). *Appl. Phys. B*, **118**, 417–429.
Mino, L., Bonino, V., Agostino, A., Prestipino, C., Borfecchia, E., Lamberti, C., Operti, L., Fretto, M., De Leo, N. & Truccato, M. (2017). *Sci. Rep.* **7**, 9066.
Mino, L., Bonino, V., Picollo, F., Fretto, M., Agostino, A. & Truccato, M. (2019). *Adv. Electron. Mater.* **5**.
Mino, L., Borfecchia, E., Segura-Ruiz, J., Giannini, C., Martinez-Criado, G. & Lamberti, C. (2018). *Rev. Mod. Phys.* **90**, 65.
Mirzoev, F. K., Panchenko, V. Y. & Shelepin, L. A. (1996). *UFN*, **166**, 3–32.
Moshe, E., Eliezer, S., Henis, Z., Werdiger, M., Dekel, E., Horovitz, Y., Maman, S., Goldberg, I. B. & Eliezer, D. (2000). *Appl. Phys. Lett.* **76**, 1555–1557.
Natividad, E., Castro, M., Burriel, R. & Angurel, L. A. (2006). *J. Therm. Anal. Calorim.* **84**, 307–316.
Neutze, R., Wouts, R., van der Spoel, D., Weckert, E. & Hajdu, J. (2000). *Nature*, **406**, 752–757.
Nicholson, J., Nave, C., Fayz, K., Fell, B. & Garman, E. (2001). *Nucl. Instrum. Methods Phys. Res. A*, **467–468**, 1380–1383.
Pagliero, A., Mino, L., Borfecchia, E., Truccato, M., Agostino, A., Pascale, L., Enrico, E., Leo, N. D., Lamberti, C. & Martínez-Criado, G. (2014). *Nano Lett.* **14**, 1583–1589.
Rosenthal, M., Doblas, D., Hernandez, J. J., Odarchenko, Y. I., Burghammer, M., Di Cola, E., Spitzer, D., Antipov, A. E.,

Aldoshin, L. S. & Ivanov, D. A. (2014). *J. Synchrotron Rad.* **21**, 223–228.
Ryutov, D. D. (2003). *Rev. Sci. Instrum.* **74**, 3722–3725.
Seitz, F. & Turnbull, D. (1956). *Solid State Physics*, pp. 307–449. New York: Academic Press.
Snell, E. H., Bellamy, H. D., Rosenbaum, G. & van der Woerd, M. J. (2007). *J. Synchrotron Rad.* **14**, 109–115.
Stanley, H. B., Banerjee, D., van Breemen, L., Ciston, J., Liebscher, C. H., Martis, V., Merino, D. H., Longo, A., Pattison, P., Peters, G. W. M., Portale, G., Sen, S. & Bras, W. (2014). *CrystEngComm*, **16**, 9331–9339.
Subramanian, M. A., Torardi, C. C., Calabrese, J. C., Gopalakrishnan, J., Morrissey, K. J., Askew, T. R., Flippen, R. B., Chowdhry, U. & Sleight, A. W. (1988). *Science*, **239**, 1015–1017.
Torsello, D., Mino, L., Bonino, V., Agostino, A., Operti, L., Borfecchia, E., Vittone, E., Lamberti, C. & Truccato, M. (2018). *Phys. Rev. Mater.* **2**, 014801.
Truccato, M., Agostino, A., Borfecchia, E., Mino, L., Cara, E., Pagliero, A., Adhlakha, N., Pascale, L., Operti, L., Enrico, E., De Leo, N., Fretto, M., Martinez-Criado, G. & Lamberti, C. (2016). *Nano Lett.* **16**, 1669–1674.
Truccato, M., Agostino, A., Rinaudo, G., Cagliero, S. & Panetta, M. (2006). *J. Phys. Condens. Matter*, **18**, 8295–8312.
Tu, F., Spath, A., Drost, M., Vollnhals, F., Calderon, S. K., Fink, R. H. & Marbach, H. (2017). *J. Vac. Sci. Technol. B*, **35**, 031601.
US Standard Atmosphere (1976). US Government Printing Office, Washington, DC.
Wallander, H. & Wallentin, J. (2017). *J. Synchrotron Rad.* **24**, 925–933.